Deep Learning Enabled Universal Multiplexed Fluorescence Detection for Point-of-Care Applications

Aneesh Kshirsagar, Anthony J. Politza, and Weihua Guan*

Cite This: *ACS Sens.* 2024, 9, 4017−4027

Read Online

| ACCESS | Metrics & More | Article Recommendations | Supporting Information |

ABSTRACT: There is a significant demand for multiplexed fluorescence sensing and detection across a range of applications. Yet, the development of portable and compact multiplexable systems remains a substantial challenge. This difficulty largely stems from the inherent need for spectrum separation, which typically requires sophisticated and expensive optical components. Here, we demonstrate a compact, lens-free, and cost-effective fluorescence sensing setup that incorporates machine learning for scalable multiplexed fluorescence detection. This method utilizes low-cost optical components and a pretrained machine learning (ML) model to enable multiplexed fluorescence sensing without optical adjustments. Its multiplexing capability can be easily scaled up through updates to the machine learning model without altering the hardware. We demonstrate its real-world application in a probe-based multiplexed Loop-Mediated Isothermal Amplification (LAMP) assay designed to simultaneously detect three common respiratory viruses within a single reaction. The effectiveness of this approach highlights the system's potential for point-of-care applications that require cost-effective and scalable solutions. The machine learning-enabled multiplexed fluorescence sensing demonstrated in this work would pave the way for widespread adoption in diverse settings, from clinical laboratories to field diagnostics.

KEYWORDS: *multiplexed fluorescence sensing, machine learning, neural network, LAMP, point-of-care, lens-free*
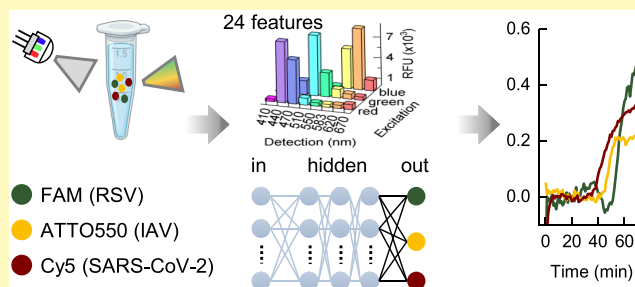
Fluorescence detection serves as a crucial readout method in a wide array of biochemical assays, including quantitative Polymerase Chain Reaction,[1] Enzyme-Linked Immunosorbent Assay,[2] and various microscopy and imaging techniques.[3,4] This prominence is attributed to the simplicity of visualizing targets once they are labeled with fluorescent tags or dyed. Traditional commercial instruments, characterized by their bulkiness and high cost, rely on interchangeable optical components like filters, dichroic mirrors, and lenses, rendering them impractical for portable applications. Nevertheless, such complex systems are not always necessary for conducting bulk fluorescence measurement assays, and more straightforward yet reliable solutions are being developed for portable use.

Point-of-care testing (POCT) represents a versatile approach to diagnostics, capable of being conducted in diverse environments such as field locations, homes, ambulances, and hospitals. POCT circumvents the constraints of conventional laboratory settings by eliminating the need for specialized personnel and enabling the rapid delivery of results, making it particularly valuable for diagnostic applications.[5,6] The advantages of POCT have spurred the development of platforms designed for real-time, quantitative, and sensitive testing, and fluorescence (optical) detection emerges as a preferred detection strategy, rivaled by other technologies like electrochemical, surface plasmon resonance (SPR), and surface-enhanced Raman scattering (SERS).[7] This preference underscores the need for

further innovation in miniaturized fluorescence measurement devices, fostering advancements that could revolutionize point-of-care diagnostics.[8]

Concurrently, there has been a focus on developing multiplexed diagnostics in point-of-care settings to conduct comprehensive analyses with minimal sample volume, aiming to reduce cost and time significantly, enhance decision-making accuracy and speed, improve patient outcomes, and streamline lab workflows.[9,10] Multiplexed testing is essential as it allows for the identification of multiple pathogens or disease indicators from a single sample and is being used in various areas. For example, the detection of renal biomarkers to indicate acute kidney damage,[11] cardiac biomarkers to identify patients with developing cardiovascular diseases,[12] cancer biomarkers for monitoring purposes,[13] and infectious disease diagnostics, wherein this capability is crucial for differentiating between diseases with similar symptoms,[14] confirming specific infections,[15] or identifying variants for epidemiological surveil-
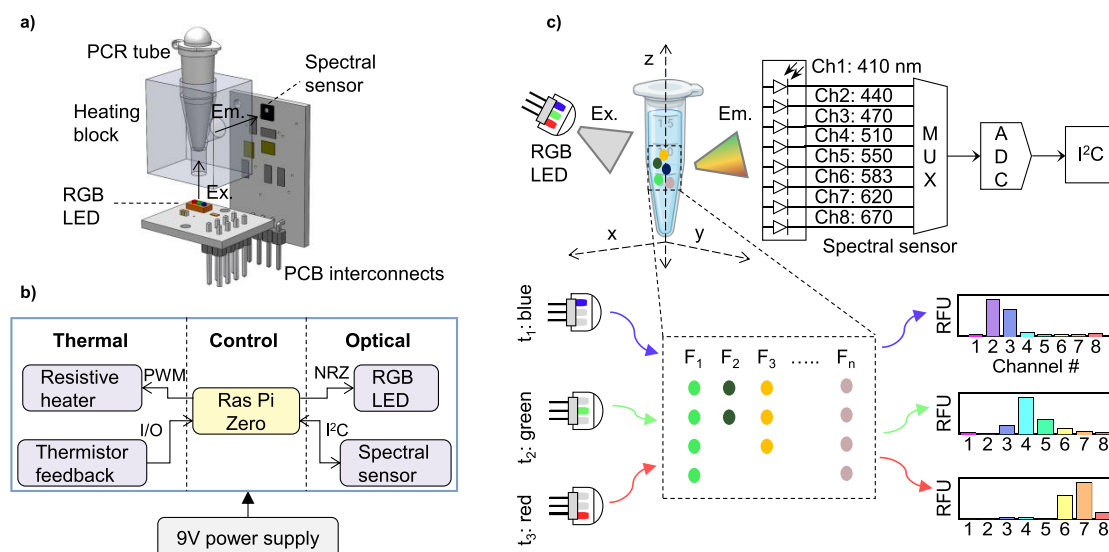
Figure 1. An overview of the optical assembly and procedure for multiplexed fluorescence detection. (a) 3D render of the optical assembly developed for multiplexed fluorescence detection. It consists of an RGB LED with red, green, and blue lights as the excitation source and a multichannel spectral sensor for detecting the collective emission, arranged perpendicular to each other to reduce excitation light leaked into the sensor. A highlight of this setup is that it forgoes a lens, which may require precise alignment and positioning to ensure emissions are focused on the sensor, hence permitting some room for alignment errors. (b) A simplified electronic block diagram of the setup shows all the components. A Raspberry Pi Zero microprocessor controls thermal and optical submodules and records the data. (c) Schematic representation of the fluorescence generation from a mixture of n fluorophores (denoted by F_1, F_2, F_3, ..., F_n) and its detection. The mixture is depicted using colored dots, where each color represents a different fluorophore. Here, $n = 4$ results in four columns, with the number of rows in each column reflecting the concentration of the corresponding fluorophore. The process involves exciting the mixture by alternating between the three sources in a time-divided manner and capturing the combinatorial emitted fluorescence for each excitation by the sensor across eight wavelength channels, facilitated by high-precision monolithic filters on top of an array of photodiodes and later converted to digital values.

lance.[16] Given the effectiveness and simplicity of fluorescence-based readouts, there's a pressing need to advance multiplexed fluorescence sensing capabilities for efficient multiplexed diagnostics.

One prevalent strategy for sample-to-answer multiplexed POCT for nucleic acid detection is to spatially parallelize the reactions and detect multiple targets separately.[17−23] However, multiplexing via parallel reactions has multiple disadvantages due to splitting a small sample volume into multiple channels or reaction zones, such as variability in analyte concentration, reduction in analyte concentration below detectable limits, and increased instrumentation complexity. The other strategy is to develop reporters specific to the analytes under consideration instead of universal dyes such that multiplexed detection can be enabled in one-pot or one reaction. Such one-pot detection can be facilitated using various readout methods, such as a smartphone,[24−27] which has uniformity issues when the phone is changed, discrete Complementary Metal-Oxide-Semiconductor (CMOS) or Charge-Coupled Device (CCD) based detectors along with LED or Laser for excitation,[28−30] which is emerging as the preferred methodology. However, the pending challenge for highly multiplexed fluorophore detection in one pot is the overlap of the respective emission spectra. This issue typically necessitates using filters, collimating lenses, or dichroic mirrors in the optical paths, increasing the complexity and restricting the combinability of fluorophores. It may also demand hardware reconfiguration if deviating from a particular combination. Consequently, there is a critical need for an easily assembled, simple-to-adjust or universally applicable, highly multiplexable, and sensitive fluorescence detection setup for point-of-care devices.

Recent advancements in machine learning (ML) and artificial intelligence (AI) have substantially improved biochemical sensing technologies, especially in the detection of multiplexed biomarkers through medical imaging and fluorescence analysis.[31] For instance, digital immunoassays now utilize computer vision-based AI to decode complex signals from microspheres, varying in color, size, and number, facilitating precise and straightforward multiplexed detection. Additionally, a deep learning-assisted programmable chip has been developed for colorimetric sweat biomarker detection. This chip uses enzyme/indicator-immobilized capsules to accurately quantify substances like glucose and lactate.[32] Furthermore, gold nanoparticles exhibit distinct aggregation behaviors in response to various buffering conditions, which can be analyzed through ML to accurately classify and quantify neurotransmitters.[33] These developments underscore the transformative impact of AI and ML in refining diagnostic methodologies and improving clinical outcomes.

In this study, we developed a highly compact, lens-free, affordable fluorescence sensing setup that enables scalable multiplexity through ML methods. With a fixed set of hardware, the setup can analyze a mixture of fluorophores with the pretrained model, significantly reducing the complexity of traditional multiplexed fluorescence sensing, which often requires reconfiguration of the optical components. We first formulated the problem of multiplexed fluorophore detection, introduced and modeled our sensing approach, and studied the ability of this setup to detect multiplexed fluorophores by establishing the single optimized detection channel for each fluorophore based on the theoretical spectra. Further, we evaluated three distinct machine learning algorithms that leverage calibration data acquired over multiple channels to

accurately predict the concentrations of these multiplexed fluorophores without considering the spectral information and demonstrated enhanced performance and scalability. Conclusively, we applied our optical assembly and ML algorithm in the specific and real-time monitoring of three targets within a multiplexed, isothermal nucleic acid amplification assay, showcasing the practical application of our developments in a complex biological context.

■ PROBLEM FORMULATION, EXPERIMENTAL SETUP, AND MODELING

To create a device capable of compact, affordable fluorescence detection with scalable multiplexity using fixed universal hardware while addressing critical challenges, including the overlap of fluorophores' emission spectra, excitation light spillover into the detection sensors, and spatial signal loss from bypassing a collimating lens, we set out to first formulate and model an innovative fluorescence sensing approach. The task of multiplexed fluorescence detection involves analyzing a mixture with n distinct fluorophores (F_1, F_2, F_3, . . ., F_n) at unknown concentrations (C_1, C_2, C_3, . . ., C_n), with the aim to determine each fluorophore's concentration.

Our strategy involves exciting the fluorophore mixture using three sources and recording the emissions by multiple wavelength channels of a spectral sensor. This is an improvement over our previous approaches, which consisted of a single blue excitation source along with a three-channel color sensor, designed for sensing a single fluorescence.[34−36] In the development of our setup, significant emphasis was placed on achieving a lens-free design. Traditional fluorescence detection systems often employ collimating lenses to focus or direct light, enhancing the detection capabilities, especially at lower concentrations. These lenses are critical for minimizing signal loss and improving the signal-to-noise ratio. However, lenses add complexity, cost, and mechanical alignment requirements to the device assembly. Our design omits the lens, simplifying the construction and significantly reducing the need for precise optical alignment. This simplification is particularly advantageous in resource-limited settings.

Figure 1a provides a detailed view of the optical setup developed to analyze an unknown mixture of multiple fluorophores that comprises an RGB LED (SK6812) as the triwavelength excitation source and a CMOS spectral sensor (AS7341) as the emission detector, mounted perpendicular to each other. The LED consists of three separate sources and the required driver circuit in a package. It can be controlled by a microprocessor such as a Raspberry Pi via nonreturn to zero (NRZ) communication protocol. The sensor has an adjustable integration time and detects incident light using eight optical channels in the visible spectral range. It communicates with a microprocessor via interintegrated circuit (I²C) communication protocol. An overview of the electronic system is given in Figure 1b. This spectral measurement is feasible due to the integration of high-precision monolithic filters onto standard CMOS silicon via nano-optic deposited interference filter technology. The sensor has a photodiode array behind the monolithic filters, and the raw measurements are fed to a 16-bit six-channel analog-to-digital converter (ADC) via a multiplexer to provide digital relative fluorescence units (RFUs). Although our system is not entirely filter-free, the integrated filters furnish it with the ingenuity to detect fluorescent emissions across various wavelength ranges without the need for any hardware reconfiguration, unlike devices that use separate glass or acrylic filters. Figure 1c illustrates this backend operation of the spectral sensor along with the schematic representation of using the three sources within the triwavelength LED one by one in a time-divided manner to probe the fluorophore mixture and record the resulting collective emission across eight different channels of the sensor. As a result, this setup may be used to measure the emissions of different fluorophores and corresponding LED excitations simultaneously without the need for any additional lenses, filters, or dichroic beam splitters that not only complicate the assembly by requiring precise alignment of components but also limit the number of fluorophores that can be detected without hardware reconfiguration.

To better understand the complex relationship between the concentration of each fluorophore in each mixture and the emission measured by each detection channel for each excitation source, we set up a mathematical model.[37] Consider there are m excitation sources (I_1 to I_m), n fluorophores with their respective concentrations in the mixture and d detection channels of the sensor, then for each excitation i, we can try to write the interaction of the excitation source I_i, fluorophore emission coefficients $[E_i]$, fluorophore concentrations $[C]$, and coupling of the n fluorophores' emissions (due to an excitation) to the detection channels $[\beta_i]$ as below.

First, we determine the contribution of each fluorophore to the emission under excitation i, weighted by its concentration

$$[EM_1\ EM_2\ EM_3\cdots EM_n] = [E_1\ E_2\ E_3\cdots E_n] \odot [C_1\ C_2\ C_3\cdots C_n] \tag{1}$$

or

$$[EM_i]_{nX1} = [E_i]_{nX1} \odot [C]_{nX1} \tag{2}$$

where $\odot$ represents element-wise matrix multiplication. Thus, $[EM_i]$ represents the emission response of each fluorophore to the ith excitation, weighted by its concentration.

Next, we distribute these emission responses to the d detection channels, considering the coupling factors in $[\beta_i]$

$$\begin{bmatrix} \beta_{1,1} & \beta_{1,2} & \cdots & \beta_{1,d} \\ \beta_{2,1} & \beta_{2,2} & \cdots & \beta_{2,d} \\ \vdots & \vdots & \ddots & \vdots \\ \beta_{n,1} & \beta_{n,2} & \cdots & \beta_{n,d} \end{bmatrix}^T . [EM_1\ EM_2\ EM_3\cdots EM_n]$$

$$= [\beta_i]^T_{nXd}. [EM_i]_{nX1} \tag{3}$$

which is equal to the detected signals, as shown below

$$[S_i]_{dX1} = [S_1\ S_2\cdots S_d] \tag{4}$$

The time-varying S_d can be written as follows, which we have previously reported[34]

$$S_d(t) = \frac{I\beta_{n,d}}{h\nu}[\alpha[C(t)]\phi_F + N_{Bi}\phi_B] \times IT \tag{5}$$

where $h\nu$ is the emitted photon's energy, α is the absorption coefficient, C is the fluorophore concentration, ϕ_F is the fluorescence quantum yield, N_{Bi} is the background signal, ϕ_B is the background signal quantum yield, and IT is the sensor's integration time.

To summarize, for each excitation i ranging between 1 to m, we can write m different equations with the following form,

$$[\beta_i]^T . ([E_i] \odot [C]) = [S_i] \tag{6}$$

and all the detected values can be arranged in another matrix as

$$[S] = \begin{bmatrix} S_{1,1} & S_{1,2} & \cdots & S_{1,d} \\ S_{2,1} & \ddots & & \vdots \\ \vdots & & \ddots & \vdots \\ S_{m,1} & \cdots & \cdots & S_{m,d} \end{bmatrix} \tag{7}$$

Thus, we have established a relationship between the detected values and corresponding fluorophore concentrations, which will be used in non-ML and ML-based analyses.

■ RESULTS AND DISCUSSION

Traditional Analytical Method. To explore the use of a conventional approach along the lines of previously reported instruments,[34,35,38,39] where a single excitation and detection channel of a sensor is used for a single fluorophore, we utilized the experimental setup described earlier. This setup detects multiple fluorophores in a mixture by choosing the optimal
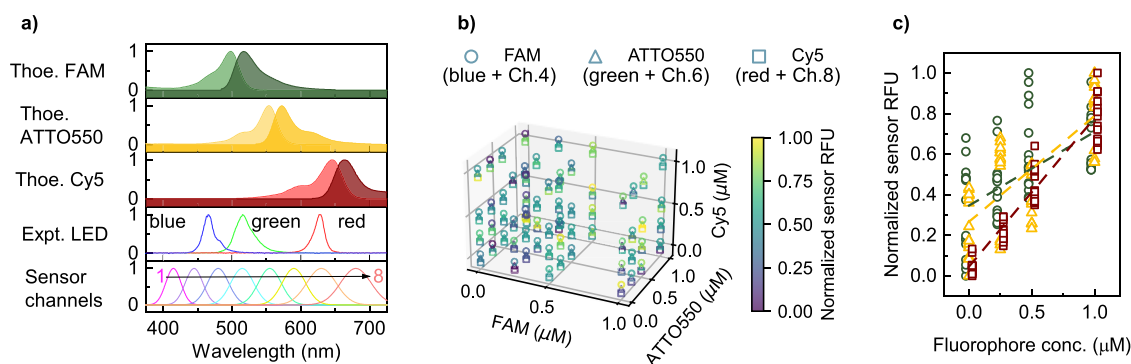
Figure 2. A traditional analytical method that uses a single source and a single detection channel per constituent fluorophore is insufficient for accurate detection. (a) Displayed are the theoretical excitation and emission spectra of the three chosen fluorophores, FAM, ATTO550, and Cy5, along with the spectra of RGB excitation sources and the sensor's eight detection channels. Blue, green, and red excitations have optimum alignment with the excitation spectra of FAM, ATTO550, and Cy5, respectively, while detection channels 4, 6, and 8 align best with their emission spectra. (b) 3D scatter plot representing the normalized sensor RFU responses to varying fluorophore concentrations in a mixture. Using the optimal excitation sources and detection channels from part a, 64 unique combinations prepared by mixing FAM, ATTO550, and Cy5 at four concentrations (0.00, 0.25, 0.50, and 1.00 μM) each were tested. This visualization shows the increasing RFU trend correlating with rising concentrations of each fluorophore, irrespective of the concentrations of the other two. (c) 2D scatter plot shows the same experimental data as in part b, mapping normalized RFUs against individual fluorophore concentrations, disregarding the concentrations of the other fluorophores in the mixture. The independent linear fits for FAM ($R^2 = 0.34$) and ATTO550 ($R^2 = 0.55$) indicate moderate linearity, suggesting difficulty in precise measurement at submicromolar concentrations. In contrast, Cy5 exhibits strong linearity ($R^2 = 0.92$), and could be due to either the better alignment of its peak excitation with the chosen source or clearer separation of its emission spectra from those of FAM and ATTO550.

excitation and detection channel combination per fluorophore based on the information about each fluorophore's excitation and emission spectra. Figure 2a shows the excitation and emission spectra of the three chosen fluorophores (FAM, ATTO550, and Cy5), along with the spectra of the excitation sources chosen for each fluorophore and their alignment with the discrete detection channels of the sensor. We can see that the blue, green, and red excitations align with FAM, ATTO550, and Cy5 excitation spectra, respectively, and we use each source one by one to excite the corresponding fluorophore that constitutes the mixture.

However, before testing a fluorophore mixture, we first need to determine which of the spectral sensor's detection channels is best for detecting each fluorophore under consideration. The alignment of the sensor's discrete detection channels with the spectral signatures of the fluorophores indicates that the highest readings captured for specific channels may stem from leakage of the LED source's incident light; this effect must be mitigated to determine the optimal detection channel for each fluorophore accurately. For this, we tested dilutions of each fluorophore individually, and the response for each detection channel is given in Supplementary Figure S1. Briefly, the plots correlating adjusted sensor responses with concentrations for FAM, ATTO550, and Cy5, when excited by blue, green, and red light, respectively, show that the channels 4, 6, and 8 centered at 510, 583, and 670 nm respectively exhibit optimal responsiveness for each dye.

After identifying the optimal detection channels for each fluorophore, we examined how one fluorophore's presence affects the others' detectability in a mixed fluorophore scenario. To test this, we prepared a sample space comprising four concentrations (0.00, 0.25, 0.50, and 1.00 μM) of each fluorophore, resulting in 64 unique combinations. These combinations and the normalized RFUs for each fluorophore's previously selected optimum channels are depicted in Figure 2b. While there is an observable upward trend in the RFUs with rising fluorophore concentrations, for a precise linear fit, we independently plot the RFUs against the concentration for each

fluorophore, disregarding the concentrations of the other two in the mixture to present the data in a clear, two-dimensional format. Figure 2c shows only moderate linearity for FAM and ATTO550, suggesting that this detection scheme may not be sufficient for accurate measurements of these fluorophores in the submicromolar range. However, the strong linearity between RFU and Cy5 concentration may be attributed to either the better alignment of Cy5's peak excitation spectra with the source or the clearer separation of Cy5's emission spectra from those of FAM and ATTO550. The higher overlap of FAM and ATTO550 spectra could complicate their distinct resolution, making it challenging to attribute Cy5's better linearity to one specific cause definitively.

Machine Learning-Based Methods. To leverage the full potential of the spectral sensor, we utilized its ability to capture emissions across multiple detection channels for the three excitation sources and simultaneously employed all the data instead of relying on optimized sources and detection channels for a particular fluorophore. By utilizing ML, we identified patterns within the data, as multiple studies have demonstrated ML's effectiveness in demixing combinatorial emissions in biological fluorescence detection and imaging.[40−42] Figure 3a depicts the implementation process of a supervised ML model initiated by collecting calibration data from 125 fluorophore mixtures. These mixtures were prepared at five specific concentrations (0.00, 0.25, 0.50, 0.75, and 1.00 μM) of FAM, ATTO550, and Cy5. For accuracy, each mixture was subjected to seven measurements under three different excitation sources, blue, green, and red, with each measurement capturing data across all eight detection channels, generating 24 RFU values. These values were then used as input features for the ML model, designed to predict the concentrations of the three distinct fluorophores concurrently. We allocated 80% of the data for training each model, while the remaining 20% was used for model validation and testing. We evaluated three types of models, multivariate linear regression (MLR), support vector regression (SVR), and a multilayer perceptron neural network
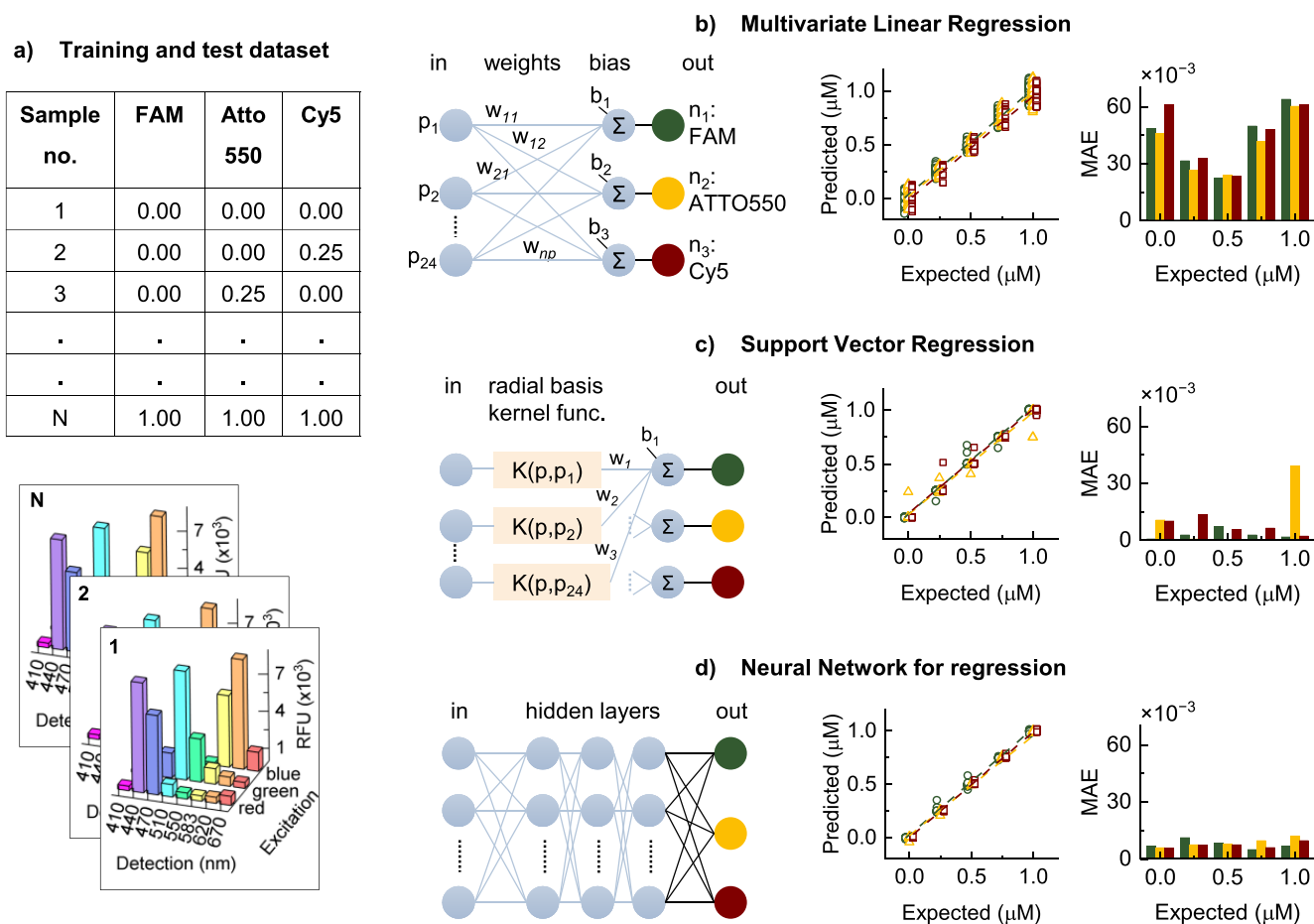
Figure 3. Comparative analysis of machine learning models for multiplexed fluorescence concentration predictions favors a Neural Network. (a) Tabular presentation of fluorophore mixture compositions (top), with a sample space of $N = 125$ mixtures using five concentrations (0.00, 0.25, 0.50, 0.75, and 1.00 μM) of each fluorophore. These samples were probed by the developed optical setup, generating 24 features—eight detection channels' values for three excitations (bottom). Each of the 125 samples was measured seven times to generate 875 data frames, and 20% of this data set is reserved for testing and validation. (b) Performance evaluation of Multivariate Linear Regression (MLR) for predicting concentrations. Left: MLR architecture; center: predicted versus expected fluorophore concentrations with linear fits having R^2 value of 0.97 for FAM, ATTO550, and Cy5; right: concentration-specific mean absolute errors (MAE) for all fluorophores, which reveal higher inaccuracies at the extremities of the concentration range (0 and 1 μM). (c) Support Vector Regression (SVR), with the model architecture (left), yields improved linear fits (center) with R^2 values of 0.99, 0.95, and 0.98 for each fluorophore and reduced MAEs (right). Despite the improvement over MLR, the nonrandom and biased accuracy points to the potential for developing a better model. (d) Neural Network (NN), with the model architecture illustrated (left), demonstrates the best predictive linearity (center) with R^2 value of 0.99 for each fluorophore and presents the lowest MAEs (right), indicating its superior ability to handle nonlinearities without biased predictive accuracy.

(NN), to determine the most effective method for accurate prediction.

Multivariate Linear Regression. To explore how each fluorophore concentration influences the emission values and ultimately predict these concentrations, we utilized the multivariate linear regression (MLR) model, as it is a foundational regression technique. Within MLR, we applied linear algebra principles to calculate the weights and biases associated with each of the 24 RFU values serving as inputs. Inspired by the previously proposed model, eq 8 illustrates the MLR model tailored for predicting the concentration of the FAM fluorophore, utilizing 24 RFU values as inputs when there are i excitations and d detection channels. In this equation, each w coefficient signifies the weight assigned to the regression parameters corresponding to each RFU input, while ε denotes the error or bias inherent in the model.

$$[C]_{FAM} = w_0 + w_{i=1,d=1}RFU_{i=1,d=1} + w_{i=1,d=2}RFU_{i=1,d=2} + \cdots + w_{i=3,d=8}RFU_{i=3,d=8} + \in_{FAM} \tag{8}$$

Similarly, two more equations can be written for ATTO550 and Cy5 to get

$$\begin{bmatrix} C_{FAM} \\ C_{ATTO550} \\ C_{Cy5} \end{bmatrix} = \begin{bmatrix} 1 & RFU_{i=1,d=1} & \cdots & RFU_{i=3,d=8} \\ 1 & RFU_{i=1,d=1} & \cdots & RFU_{i=3,d=8} \\ 1 & RFU_{i=1,d=1} & \cdots & RFU_{i=3,d=8} \end{bmatrix} \cdot \begin{bmatrix} w_0 \\ w_{i=1,d=1} \\ \vdots \\ w_{i=3,d=8} \end{bmatrix}$$
$$+ \begin{bmatrix} \in_{FAM} \\ \in_{ATTO550} \\ \in_{Cy5} \end{bmatrix} \tag{9}$$

For clarity and efficiency, tackling a multivariate regression challenge involves decomposing it into several single-variable linear regression models. In this approach, we created three distinct models, each dedicated to one of the three fluorophores, with the predictive outcomes showcased in Figure 3b. The linear correlations between predicted and actual fluorophore concentrations demonstrate a good linear relationship and proficient predictive capabilities for static concentrations. Additionally, residual analysis for each fluorophore, detailed in Supplementary Figure S2, reveals a normal distribution of residuals, affirming our model's assumption of homoscedasticity - constant variance around a zero mean. Despite these promising indicators, the concentration-specific mean absolute errors (MAE) unveil pronounced inaccuracies at the lowest and highest concentration levels (0 and 1 μM). This observation indicates the model's difficulty in effectively handling the entire concentration range, potentially due to nonlinearities like overlapping emission spectra and secondary excitations. Thus, we were motivated to explore more advanced machine learning models capable of addressing nonlinear relationships to improve predictive accuracy across all concentrations.

Support Vector Regression. Support vector machines (SVM) perform the nonlinear mapping of input vectors into a high-dimensional feature space and use a linear decision surface within this feature space primarily for binary classification.[43,44] Given the potential nonlinearities mentioned in the previous section, SVM could perhaps be a better candidate for predicting the fluorophore concentrations in a mixture. Here, a hyperplane within the feature space acts as the optimal boundary, set by an error margin, with support vectors crucial for its positioning based on data outliers. Support Vector Regression (SVR), utilizing kernel functions like the radial basis function (RBF), adapts the basic framework of SVM for regression problems and handles nonlinear data by striving for the best fit within a specific error threshold rather than minimizing prediction errors directly.

Considering SVR's limitation with multiple outputs, we crafted three distinct SVR models with the RBF kernel to estimate the concentrations of three fluorophores, presenting these findings in Figure 3c. Comparing the linear correlations between predicted and actual concentrations of FAM, ATTO550, and Cy5, we observed a marked advancement over MLR, as also evidenced by the substantially decreased MAEs. Further, despite changing the kernel function to linear and sigmoid, RBF, along with hyperparameter tuning such as the penalty parameter (C), the kernel coefficient (γ), and epsilon in the loss function (ϵ), performed the best. Yet the nonrandom and biased accuracy hints at the potential for the exploration of additional ML models capable of handling a higher degree of nonlinearity.

Neural Network. Neural networks (NN) process input data across multiple layers, where each neuron performs a weighted sum of its inputs, followed by a nonlinear activation function, enabling the network to capture intricate data patterns.[45] Here, we use a multilayer perceptron (MLP), a feedforward artificial neural network (ANN) implementing supervised learning, and the output layer generates predictions that are evaluated against true values to determine errors. These errors are then propagated backward to adjust neuron weights during the training phase. Given their layered architecture and nonlinear activation functions, we expect NN to outperform SVR in this application by more effectively modeling complex, nonlinear, and hierarchical relationships within the data. Figure 3d

illustrates the NN's predictions for FAM, ATTO550, and Cy5 fluorophores, showing a notable enhancement in the correlation between predicted and actual concentrations compared to SVR. Furthermore, the MAE for each concentration level is marginally lower than that observed with SVR, without indicating any biased accuracy.

Performance Comparison between Non-ML and ML Methods. To explain why the ML methods perform much better than an optimized channel's readings, we consider eq 6, which gives us an empirical relation assuming a linear superposition of emissions and detection responses. However, measuring the exact emission response of each fluorophore to each excitation and the distribution of the emission responses over the detection channels is challenging, and valuable emission information may be lost by choosing a single detection channel. In addition, the nonlinear effects, such as overlapping emission spectra and leakage of excitations due to the exclusion of filters, cannot be effectively measured or defined. This makes the accurate development of a model challenging while considering all these intricacies, and it may explain the inadequacy of using a single excitation source and an optimum detection channel for sensing fluorophores present in a mixture.

The underlying principle of the supervised machine learning approach involves forming a data set with various combinations of constituent fluorophores at specific concentrations, and recording the resultant fluorescent emissions across eight channels. Each channel is responsive to specific wavelength ranges, corresponding to three separate excitation lights. This data helps to train a model that establishes a complex relationship between the concentrations of multiple fluorophores and the fluorescence readings measured by the sensor. This model can then predict the concentrations of fluorophores in an unknown sample based on these readings. The model incorporates crucial data about the predominant influence of certain fluorophores over specific detection channels and uses this information to predict concentrations from a set of measured readings. It also models the concentration-specific cross-influence within the prediction algorithm. Due to the extensive training data set featuring unique combinations, the model predicts concentrations for combinations of fluorophores, rather than individual ones. When used in conjunction with specific probe-based biochemical reactions, where the concentration of a targeted fluorophore increases (if the target is present) while other fluorophores remain stable, this approach effectively prevents signal cross-influence.

Performance Comparison among ML Methods. To find the most accurate ML model, we compare the performance of the three models among each other and with the optimized channel method through metrics such as the R^2, mean absolute error (MAE), limit of detection (LoD), and limit of quantification (LoQ) values in Table 1. Please refer to Materials and Methods for details regarding the calculation of LoD and LoQ. The NN model surpasses others in predictive accuracy, making it the preferred choice for further exploration in real-world applications, such as nucleic acid amplification assays. It should be noted that the observed improvements in the LoD and LoQ are primarily due to the NN's enhanced ability to model the complex interactions among fluorophores, which are expected to be predominantly nonlinear.

To establish the relevance of the error values, we consider the maximum fluorophore concentration used in our experiments to construct the training and test data set: 1 μM. This value is used to convert the MAEs to percentage errors in Table 1. To

Table 1. Performance Comparison of Fluorescence Detection Methods

Fluorophore	R^2	% MAE	LoD (μM)	LoQ (μM)
Optimized Source and Channel Response Method				
FAM	0.35	NA	1.60	5.26
ATTO550	0.56	NA	1.07	3.52
Cy5	0.93	NA	0.18	0.58
Multivariate Linear Regression				
FAM	0.97	4.33	0.15	0.48
ATTO550	0.97	3.98	0.16	0.54
Cy5	0.97	4.54	0.19	0.63
Support Vector Regression				
FAM	0.99	0.50	0.03	0.01
ATTO550	0.95	1.18	0.01	0.38
Cy5	0.98	1.00	0.07	0.25
Multilayer Perceptron (NN) Regression				
FAM	0.99	1.99	0.03	0.10
ATTO550	0.99	0.66	0.02	0.09
Cy5	0.99	0.67	0.02	0.06

understand how this percentage MAE affects the prediction of the final target concentration, we would need to empirically determine two relationships: (i) between fluorophore concentration and time to positive (TTP), and (ii) the standard curve equation for target concentration in a biochemical reaction. Therefore, we report the MAE in terms of percentage. Please note that the observed improvements in MAE, LoD, and LoQ do not directly imply an enhancement in the spectral sensor's intrinsic electronic sensitivity to weaker signals. Additionally, the LoD of a fluorophore could vary under different background concentrations of the other two fluorophores. However, a comprehensive evaluation in a three-dimensional space involving all possible fluorophore combinations would lead to

a prohibitively high number of experimental conditions, making practical validation infeasible. Hence, in Supplementary Table S1, we present a comparison of the best-case (where the concentration of the other two fluorophores is the lowest, i.e., 0 μM) and worst-case (where the concentration of the other two fluorophores is the highest, i.e., 1 μM) scenarios. The results do not demonstrate a significant worsening of the MAE, LoD, and LoQ values as the background concentrations of the fluorophores increase.

Scalable Multiplexity Enabled by ML. To illustrate the setup's scalability for varying number of fluorophores in the mixture, we assessed its performance in predicting concentrations of two, three, or four fluorophores. We used four different concentrations (0.00, 0.25, 0.50, 1.00 μM) of each fluorophore, resulting in 16 combinations for ATTO425 and FAM, 64 combinations for ATTO425, FAM and ATTO550, 256 combinations for ATTO425, FAM, ATTO550, and Cy5. As before, each mixture underwent seven measurements at blue, green, and red excitations while detections were recorded across eight detection channels to generate 24 RFU values, which served as inputs for the NN model tasked with predicting the concentrations of the constituent fluorophores, using 80% of the data for training and 20% for validation and testing. The results, illustrated in Figures 4a, 4b, and 4c for two, three, and four fluorophores, respectively, show the predicted versus actual concentrations for each fluorophore along with the MAEs. The marginal improvement in prediction linearity and concentration-specific MAEs is likely due to the increased training and test samples as the number of fluorophores increases. No significant trends across concentrations within each model indicate uniform predictive reliability. This demonstrates the scalability of our setup to accommodate mixtures with varying
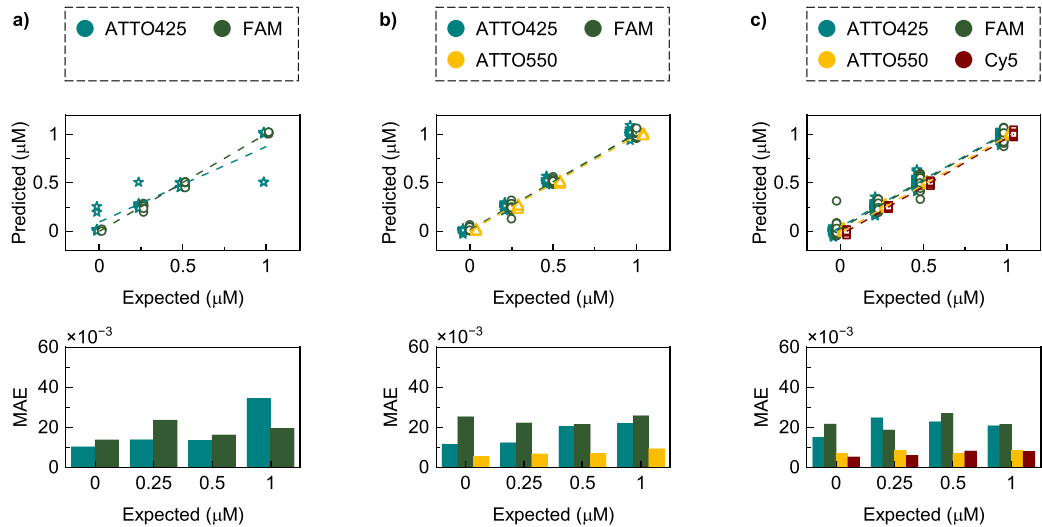

Figure 4. Scalable multiplexed fluorophore detection using a Neural Network model without hardware reconfiguration. (a) The evaluation of NN for predicting concentrations in two-fluorophore mixtures consisting of ATTO425 and FAM (top) with four concentration levels (0.00, 0.25, 0.50, and 1.00 μM), resulting in 16 combinations. Samples were probed seven times, with the resulting data set split into 80% for training and 20% for testing. The predictions (middle) have R^2 values of 0.99 for ATTO425 and 0.81 for FAM, and corresponding concentration-specific MAEs displayed (bottom). (b) The concentration predictions for 64 three-fluorophore mixtures of ATTO425, FAM, and ATTO550 (top) demonstrate improved predictive linearity (middle) with R^2 values of 0.99 for all fluorophores, and corresponding MAEs (bottom). (c) The concentration predictions for 256 four-fluorophore mixtures of ATTO425, FAM, ATTO550, and Cy5 (top) display predictive linearity (middle) while maintaining R^2 values of 0.99 for all fluorophores, and corresponding MAEs (bottom), consistent with the three-fluorophore model. The lower performance of the two-fluorophore model is due to its smaller data set. Comparable predictive reliability for each fluorophore across models confirms the capability to handle mixtures with different numbers of fluorophores.
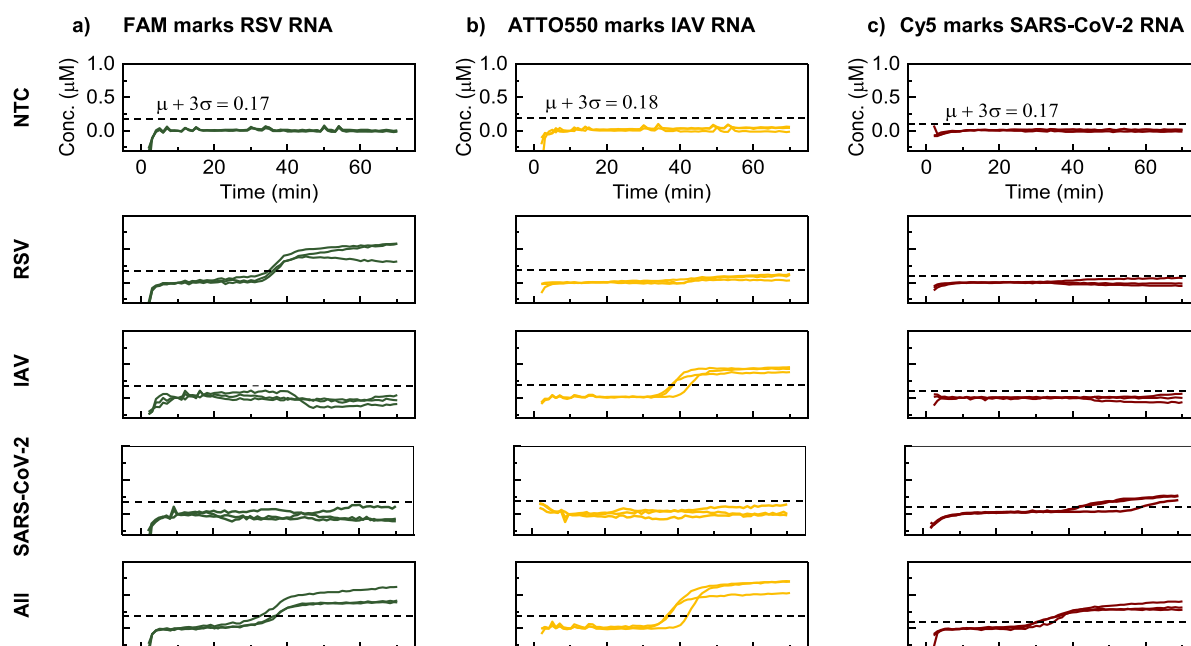
Figure 5. Demonstrating the use of the machine learning-enhanced fluorescence detection setup for a biochemical assay. (a) The real-time amplification curves for FAM fluorophore, indicating the presence of RSV RNA in a triplex reverse-transcription loop-mediated isothermal assay (RT-LAMP) for five different samples (in triplicates): no template control (NTC), RSV RNA only, IAV RNA only, SARS-CoV-2 RNA only, and a combination of all three RNAs. The curves represent offline-predicted fluorophore concentrations using the 24 feature values acquired at 30-s intervals, with the horizontal dotted line denoting a threshold concentration T_C, calculated as the mean (μ) plus three standard deviations (3σ) of the NTC reactions. (b) and (c) present the real-time amplification curves for ATTO550 (b) and Cy5 (c) fluorophores, tracing IAV and SARS-CoV-2 RNA detection in the same triplex reactions. The appropriate amplification of each RNA across the samples validates the optical setup's suitability for practical assay deployment.

fluorophores without requiring reconfiguration of the optical components.

Example Application for Real-Time RT-LAMP Detection. Having demonstrated the capability of our optical setup, in conjunction with NN modeling, to predict static fluorophore concentrations within a mixture accurately, we applied this system to track the progression of a real-world biochemical diagnostic assay as a test-bed. The technique in focus, Loop-mediated Isothermal Amplification (LAMP), was initially introduced by Notomi et al.[46] to amplify DNA molecules exponentially under isothermal conditions. We made use of a Reverse Transcription LAMP (RT-LAMP) assay for the simultaneous detection of the presence of three RNA targets: Respiratory Syncytial Virus (RSV), Influenza A (IAV), and Severe Acute Respiratory Syndrome Coronavirus-2 (SARS-CoV-2). Here, multiplexed detection was enabled by the Detection of Amplification by Release of Quenching (DARQ) technique,[47] which involves the unquenching of fluorescently labeled probes upon the extension of the backward strand to produce an increasing amount of specific fluorescence as the amplification proceeds. In addition to enabling multiplexed detection, DARQ LAMP also enables higher specificity, which helps in alleviating false positives in traditional intercalating dye-based LAMP that is often considered a characteristic drawback.

The concentration of each RNA target was 1500 copies per reaction (cp/rxn), and five distinct combinations were introduced into the multiplexed reaction, viz., the no template control (NTC), the three individual targets (RSV, IAV, and SARS-CoV-2), and a mixture of all three targets. These targets were added to triplicate reactions that were subsequently incubated at 61 °C for 70 min and then swiftly cooled to room temperature to stop the amplification. The raw fluorescence data

acquired by the optical assembly at 30-s intervals was supplied to the NN model described earlier to predict the time-varying concentration for each constituent fluorophore in an offline manner. Figures 5a, 5b and 5c show the concentrations of FAM, ATTO550, and Cy5 as a function of time, which mark the amplification and detection of RSV, IAV, and SARS-CoV-2, respectively. A threshold concentration T_C was computed based on the NTC reactions such that $T_C = \mu + 3\sigma$, where μ and σ represent the mean and standard deviation of concentrations over the entire reaction time, and a positive call was made when the predicted concentration surpasses the set threshold. All plots show accurate prediction of amplification in conditions where the RNA target was present individually or with other targets, thus validating the proposed optical assembly and accompanying NN model for monitoring the change in a multiplexed nucleic acid amplification and detection assay. The use of fluorophores in LAMP assays provides a visual or measurable indicator of the amplification process with high specificity. The relationship between the increase in fluorescence intensity and the amount of target RNA amplified is linear up to a phase before saturation occurs due to the unavailability of additional fluorophore attached primer. Consequently, quantifying the initial target sample is feasible by measuring the time to positive and establishing a standard curve, where a shorter time to positive typically indicates a higher initial target concentration. While this study highlights the foundational detection mechanisms and ML integration for multiplexed target detection, we note that extensive further testing will be required to fully evaluate the sensitivity, specificity, and quantitative capabilities of the assay for each target before deploying it in real-world human infection scenarios. Characterization of these aspects is underway, and findings will be presented in

subsequent publications based on the detection systems introduced here.

CONCLUSION

Our study introduces a transformative approach to fluorescence measurement for point-of-care applications involving bulk assays via a lens-free optical assembly complemented by a machine learning model. The effective deployment of a Neural Network to analyze data from mixtures excited by a triwavelength source and the emissions detected by eight channels of a spectral sensor significantly enhances detection and quantification limits beyond traditional single-channel approaches. The scalability of our model highlights its capability to advance point-of-care diagnostics, offering a versatile, highly multiplexable solution without the need for intricate reconfigurations for diverse fluorophores or targets. Validating its utility in concurrently detecting viral RNA from pathogens like RSV, Influenza A, and SARS-CoV-2 underscores its potential in addressing urgent needs for multiplexed biomarker detection across critical health areas. Future efforts will concentrate on refining the ML model for a more straightforward incorporation of new fluorophores using only their specific calibration data without requiring the preparation and testing of exponential unique fluorophore combinations, thereby simplifying the process.

MATERIALS AND METHODS

Design and Fabrication. The aluminum heating block and adapter for mounting the RGB LED and spectral sensor were designed using Solidworks CAD software, while the printed circuit boards (PCBs) for the LED and sensor were designed with AutoDesk Eagle CAD. All components of the optical setup were virtually assembled in Solidworks to verify alignment prior to fabrication. The heating block was machined by Protolabs Network, and the adapter was 3D printed in-house using a MakerBot MethodX printer (Brooklyn, NY) with ABS material. The PCBs were fabricated by OSH Park LLC (Lake Oswego, OR). The RGB LED (SK6812) was sourced from Adafruit Industries (New York, NY), and other components such as the spectral sensor (AS7341), a two-ohm power resistor (MP725−2.00) for heating, a 10k-ohm thermistor (MC65F103A) for temperature feedback, and a Raspberry Pi Zero microprocessor were purchased from DigiKey.com. A detailed description and function of each component, along with a cost estimate, are provided in Supplementary Table S2.

Data Set and Codes for ML Model Training and Concentration Prediction in Python. The training data sets referenced in sections concerning the analysis and comparison of ML-based methods and the scalability enabled by ML, along with the corresponding Python codes to generate, train, and test the ML models that were subsequently evaluated for predicting static fluorophore combinations are available in a GitHub repository. While developing the ML models, we made use of the SciPy open-source package for developing Multiple Linear Regression and Scikit-learn package for Support Vector Regression and Neural Network models and developed custom codes to train the specific models, pre- and postprocess the data and generate prediction results and associated figures. These resources can be accessed at https://github.com/alk5897/ML-aided-optics-for-POC-multiplexed-fluorescence.

Calculation of LoB, LoD, and LoQ Values. The limit of blank (LoB) was determined using the formula: $\mu_{blank} + 1.64*(\sigma_{blank})$, where μ_{blank} and σ_{blank} are the mean and standard deviation of the predictions at 0 μM, respectively. The limit of detection (LoD) was then defined as LoB + 1.62 × ($\sigma_{0.25}$), where $\sigma_{0.25}$ is the standard deviation of predictions at a low concentration of 0.25 μM. The limit of quantification (LoQ) was calculated as 3.3 × LoD.[48] For the traditional analytical approach using a single optimal detection channel, we first calculated the LoB, LoD, and LoQ values in terms of relative fluorescence units (RFU). We then applied the linear fit equations from Figure 2c: $RFU_{FAM} = (0.36) \times$

$C_{FAM} + 0.34$, $RFU_{ATTO550} = (0.52) \times C_{ATTO550} + 0.26$, and $RFU_{Cy5} = (0.73) \times C_{Cy5} + 0.04$, where C_{FAM}, $C_{ATTO550}$, and C_{Cy5} are the concentrations of FAM, ATTO550, and Cy5, respectively, to convert these values to concentrations.

RT-LAMP Reaction Mix. The RT-LAMP reaction mix consists of 1x isothermal buffer (20 mM Tris-HCl, 10 mM $(NH_4)_2SO_4$, 50 mM KCl, 2 mM $MgSO_4$, 0.1% Tween 20, pH 8.8), 3 sets of 6 primers each, 0.5 M Betain, 6 mM $MgSO_4$, 1.4 mM deoxyribonucleotide triphosphates (dNTPs), 0.5 U/μL Bst 2.0 DNA polymerase, 0.3 U/μL WarmStart reverse transcriptase, 1.5 μL purified RNA template (per target) and PCR-grade water to bring total reaction volume to 25 μL. Isothermal buffer, DNA polymerase, reverse transcriptase, dNTPs, and PCR-grade water were purchased from New England Biolabs (MA, USA). Heat-inactivated SARS-CoV-2 (VR-1986HK) RNA and quantitative genomic RNAs of Influenza A virus (H1N1) strain A/PR/8/34 (VR-95DQ) and human Respiratory Syncytial Virus strain A2 (VR-1540DQ) were purchased from American Type Culture Collection (ATCC). Primer sequences initially described in[49−51] and modified according to DARQ rules are detailed in Supplementary Table S3 and were synthesized by Integrated DNA Technologies (Coralville, USA). The three fluorophore-attached oligonucleotide sequences, Fds, were used to acquire the ML algorithms' static calibration data.

ASSOCIATED CONTENT

Supporting Information

The Supporting Information is available free of charge at https://pubs.acs.org/doi/10.1021/acssensors.4c00860.

Comprehensive analysis of sensor channel responses to identify optimal detection channel for a particular fluorophore, detailed residual analyses of machine learning models for accuracy assessment, alongside tables with a scenario-based comparison of MAE, LoD, and LoQ for the ML-based fluorescence prediction methods, cost estimate and detailed sequences of RT-LAMP primers used in the study (PDF)

AUTHOR INFORMATION

Corresponding Author

Weihua Guan — *Department of Electrical Engineering, The Pennsylvania State University, University Park, Pennsylvania 16802, United States; Department of Biomedical Engineering, The Pennsylvania State University, University Park, Pennsylvania 16802, United States;* orcid.org/0000-0002-8435-9672; Email: wzg111@psu.edu

Authors

Aneesh Kshirsagar — *Department of Electrical Engineering, The Pennsylvania State University, University Park, Pennsylvania 16802, United States;* orcid.org/0000-0003-2288-5439

Anthony J. Politza — *Department of Biomedical Engineering, The Pennsylvania State University, University Park, Pennsylvania 16802, United States;* orcid.org/0009-0005-8670-2357

Complete contact information is available at:
https://pubs.acs.org/10.1021/acssensors.4c00860

Notes

The authors declare no competing financial interest.

■ REFERENCES

(1) Bustin, S. A. Real-Time, Fluorescence-Based Quantitative PCR: A Snapshot of Current Procedures and Preferences. *Expert Rev. Mol. Diagn.* **2005**, *5* (4), 493−498.

(2) Peng, P.; Liu, C.; Li, Z.; Xue, Z.; Mao, P.; Hu, J.; Xu, F.; Yao, C.; You, M. Emerging ELISA Derived Technologies for *in Vitro* Diagnostics. *TrAC Trends Anal. Chem.* **2022**, *152*, 116605.

(3) Datta, R.; Heaster, T. M.; Sharick, J. T.; Gillette, A. A.; Skala, M. C. Fluorescence Lifetime Imaging Microscopy: Fundamentals and Advances in Instrumentation, Analysis, and Applications. *J. Biomed. Opt.* **2020**, *25* (7), 071203.

(4) Herman, B. *Fluorescence Microscopy*; Garland Science: 2020. DOI: 10.1201/9781003077060.

(5) Manmana, Y.; Kubo, T.; Otsuka, K. Recent Developments of Point-of-Care (POC) Testing Platform for Biomolecules. *TrAC Trends Anal. Chem.* **2021**, *135*, 116160.

(6) Gubala, V.; Harris, L. F.; Ricco, A. J.; Tan, M. X.; Williams, D. E. Point of Care Diagnostics: Status and Future. *Anal. Chem.* **2012**, *84* (2), 487−515.

(7) Wang, C.; Liu, M.; Wang, Z.; Li, S.; Deng, Y.; He, N. Point-of-Care Diagnostics for Infectious Diseases: From Methods to Devices. *Nano Today* **2021**, *37*, 101092.

(8) Shin, Y.-H.; Gutierrez-Wing, M. T.; Choi, J.-W. Review—Recent Progress in Portable Fluorescence Sensors. *J. Electrochem. Soc.* **2021**, *168* (1), 017502.

(9) Deshpande, A.; White, P. S. Multiplexed Nucleic Acid-Based Assays for Molecular Diagnostics of Human Disease. *Expert Rev. Mol. Diagn.* **2012**, *12* (6), 645−659.

(10) Dincer, C.; Bruch, R.; Kling, A.; Dittrich, P. S.; Urban, G. A. Multiplexed Point-of-Care Testing - xPOCT. *Trends Biotechnol.* **2017**, *35* (8), 728−742.

(11) Zhang, X.; Gibson, B.; Mori, R.; Snow-Lisy, D.; Yamaguchi, Y.; Campbell, S. C.; Simmons, M. N.; Daly, T. M. Analytical and Biological Validation of a Multiplex Immunoassay for Acute Kidney Injury Biomarkers. *Clin. Chim. Acta* **2013**, *415*, 88−93.

(12) Boonkaew, S.; Jang, I.; Noviana, E.; Siangproh, W.; Chailapakul, O.; Henry, C. S. Electrochemical Paper-Based Analytical Device for Multiplexed, Point-of-Care Detection of Cardiovascular Disease Biomarkers. *Sens. Actuators B Chem.* **2021**, *330*, 129336.

(13) Wu, Y.; Xue, P.; Kang, Y.; Hui, K. M. Paper-Based Microfluidic Electrochemical Immunodevice Integrated with Nanobioprobes onto Graphene Film for Ultrasensitive Multiplexed Detection of Cancer Biomarkers. *Anal. Chem.* **2013**, *85* (18), 8661−8668.

(14) Zhang, N.; Wang, L.; Deng, X.; Liang, R.; Su, M.; He, C.; Hu, L.; Su, Y.; Ren, J.; Yu, F.; Du, L.; Jiang, S. Recent Advances in the Detection of Respiratory Virus Infection in Humans. *J. Med. Virol.* **2020**, *92* (4), 408−417.

(15) Johnson, M.; Wagstaffe, H. R.; Gilmour, K. C.; Mai, A. L.; Lewis, J.; Hunt, A.; Sirr, J.; Bengt, C.; Grandjean, L.; Goldblatt, D. Evaluation of a Novel Multiplexed Assay for Determining IgG Levels and Functional Activity to SARS-CoV-2. *J. Clin. Virol.* **2020**, *130*, 104572.

(16) Wang, H.; Miller, J. A.; Verghese, M.; Sibai, M.; Solis, D.; Mfuh, K. O.; Jiang, B.; Iwai, N.; Mar, M.; Huang, C.; Yamamoto, F.; Sahoo, M. K.; Zehnder, J.; Pinsky, B. A. Multiplex SARS-CoV-2 Genotyping Reverse Transcriptase PCR for Population-Level Variant Screening and Epidemiologic Surveillance. *J. Clin. Microbiol.* **2021**, *59* (8), 1.

(17) Ackerman, C. M.; Myhrvold, C.; Thakku, S. G.; Freije, C. A.; Metsky, H. C.; Yang, D. K.; Ye, S. H.; Boehm, C. K.; Kosoko-Thoroddsen, T.-S. F.; Kehe, J.; Nguyen, T. G.; Carter, A.; Kulesa, A.; Barnes, J. R.; Dugan, V. G.; Hung, D. T.; Blainey, P. C.; Sabeti, P. C. Massively Multiplexed Nucleic Acid Detection with Cas13. *Nature* **2020**, *582* (7811), 277−282.

(18) Choi, G.; Prince, T.; Miao, J.; Cui, L.; Guan, W. Sample-to-Answer Palm-Sized Nucleic Acid Testing Device towards Low-Cost Malaria Mass Screening. *Biosens. Bioelectron.* **2018**, *115*, 83−90.

(19) Ji, M.; Xia, Y.; Loo, J.; Li, L.; Ho, H.-P.; He, J.; Gu, D. Automated Multiplex Nucleic Acid Tests for Rapid Detection of SARS-CoV-2, Influenza A and B Infection with Direct Reverse-Transcription Quantitative PCR (dirRT-qPCR) Assay in a Centrifugal Microfluidic Platform. *RSC Adv.* **2020**, *10* (56), 34088−34098.

(20) Rombach, M.; Hin, S.; Specht, M.; Johannsen, B.; Luddecke, J.; Paust, N.; Zengerle, R.; Roux, L.; Sutcliffe, T.; Peham, J. R.; Herz, C.; Panning, M.; Donoso Mantke, O.; Mitsakakis, K. RespiDisk: A Point-of-Care Platform for Fully Automated Detection of Respiratory Tract Infection Pathogens in Clinical Samples. *Analyst* **2020**, *145* (21), 7040−7047.

(21) Selck, D. A.; Karymov, M. A.; Sun, B.; Ismagilov, R. F. Increased Robustness of Single-Molecule Counting with Microfluidics, Digital Isothermal Amplification, and a Mobile Phone versus Real-Time Kinetic Measurements. *Anal. Chem.* **2013**, *85* (22), 11129−11136.

(22) Yeh, E.-C.; Fu, C.-C.; Hu, L.; Thakur, R.; Feng, J.; Lee, L. P. Self-Powered Integrated Microfluidic Point-of-Care Low-Cost Enabling (SIMPLE) Chip. *Sci. Adv.* **2017**, *3* (3), No. e1501645.

(23) Zhang, L.; Ding, B.; Chen, Q.; Feng, Q.; Lin, L.; Sun, J. Point-of-Care-Testing of Nucleic Acids by Microfluidics. *TrAC Trends Anal. Chem.* **2017**, *94*, 106−116.

(24) Akarapipad, P.; Bertelson, E.; Pessell, A.; Wang, T.-H.; Hsieh, K. Emerging Multiplex Nucleic Acid Diagnostic Tests for Combating COVID-19. *Biosensors* **2022**, *12* (11), 978.

(25) Ning, B.; Yu, T.; Zhang, S.; Huang, Z.; Tian, D.; Lin, Z.; Niu, A.; Golden, N.; Hensley, K.; Threeton, B.; Lyon, C. J.; Yin, X.-M.; Roy, C. J.; Saba, N. S.; Rappaport, J.; Wei, Q.; Hu, T. Y. A Smartphone-Read Ultrasensitive and Quantitative Saliva Test for COVID-19. *Sci. Adv.* **2021**, *7* (2), No. eabe3703.

(26) Priye, A.; Wong, S.; Bi, Y.; Carpio, M.; Chang, J.; Coen, M.; Cope, D.; Harris, J.; Johnson, J.; Keller, A.; Lim, R.; Lu, S.; Millard, A.; Pangelinan, A.; Patel, N.; Smith, L.; Chan, K.; Ugaz, V. M. Lab-on-a-Drone: Toward Pinpoint Deployment of Smartphone-Enabled Nucleic Acid-Based Diagnostics for Mobile Health Care. *Anal. Chem.* **2016**, *88* (9), 4651−4660.

(27) Wei, Q.; Luo, W.; Chiang, S.; Kappel, T.; Mejia, C.; Tseng, D.; Chan, R. Y. L.; Yan, E.; Qi, H.; Shabbir, F.; Ozkan, H.; Feng, S.; Ozcan, A. Imaging and Sizing of Single DNA Molecules on a Mobile Phone. *ACS Nano* **2014**, *8* (12), 12725−12733.

(28) Blumenfeld, N. R.; Bolene, M. A. E.; Jaspan, M.; Ayers, A. G.; Zarrandikoetxea, S.; Freudman, J.; Shah, N.; Tolwani, A. M.; Hu, Y.; Chern, T. L.; Rogot, J.; Behnam, V.; Sekhar, A.; Liu, X.; Onalir, B.; Kasumi, R.; Sanogo, A.; Human, K.; Murakami, K.; Totapally, G. S.; Fasciano, M.; Sia, S. K. Multiplexed Reverse-Transcriptase Quantitative Polymerase Chain Reaction Using Plasmonic Nanoparticles for Point-of-Care COVID-19 Diagnosis. *Nat. Nanotechnol.* **2022**, *17* (9), 984−992.

(29) Trick, A. Y.; Chen, F.-E.; Chen, L.; Lee, P.-W.; Hasnain, A. C.; Mostafa, H. H.; Carroll, K. C.; Wang, T.-H. Point-of-Care Platform for Rapid Multiplexed Detection of SARS-CoV-2 Variants and Respiratory Pathogens. *Adv. Mater. Technol.* **2022**, *7* (6), 2101013.

(30) Xun, G.; Lane, S. T.; Petrov, V. A.; Pepa, B. E.; Zhao, H. A Rapid, Accurate, Scalable, and Portable Testing System for COVID-19 Diagnosis. *Nat. Commun.* **2021**, *12* (1), 2905.

(31) Li, H.; Xu, H.; Li, Y.; Li, X. Application of Artificial Intelligence (AI)-Enhanced Biochemical Sensing in Molecular Diagnosis and Imaging Analysis: Advancing and Challenges. *TrAC Trends Anal. Chem.* **2024**, *174*, 117700.

(32) Liu, Z.; Li, J.; Li, J.; Yang, T.; Zhang, Z.; Wu, H.; Xu, H.; Meng, J.; Li, F. Explainable Deep-Learning-Assisted Sweat Assessment via a Programmable Colorimetric Chip. *Anal. Chem.* **2022**, *94* (45), 15864−15872.

(33) Hassani-Marand, M.; Fahimi-Kashani, N.; Hormozi-Nezhad, M. R. Machine-Learning Assisted Multiplex Detection of Catecholamine Neurotransmitters with a Colorimetric Sensor Array. *Anal. Methods* **2023**, *15* (9), 1123−1134.

(34) Kshirsagar, A.; Choi, G.; Santosh, V.; Harvey, T.; Bernhards, R. C.; Guan, W. Handheld Purification-Free Nucleic Acid Testing Device for Point-of-Need Detection of Malaria from Whole Blood. *ACS Sens.* **2023**, *8* (2), 673−683.

(35) Liu, T.; Choi, G.; Tang, Z.; Kshirsagar, A.; Politza, A. J.; Guan, W. Fingerpick Blood-Based Nucleic Acid Testing on A USB Interfaced Device towards HIV Self-Testing. *Biosens. Bioelectron.* **2022**, *209*, 114255.

(36) Tang, Z.; Cui, J.; Kshirsagar, A.; Liu, T.; Yon, M.; Kuchipudi, S. V.; Guan, W. SLIDE: Saliva-Based SARS-CoV-2 Self-Testing with RT-LAMP in a Mobile Device. *ACS Sens.* **2022**, *7* (8), 2370−2378.

(37) Choi, Y. J.; Takahashi, K.; Misawa, N.; Hizawa, T.; Iwata, T.; Sawada, K. Multi-Wavelength Fluorescence Detection of Submicro-molar Concentrations Using a Filter-Free Fluorescence Sensor. *Sens. Actuators B Chem.* **2018**, *256*, 38−47.

(38) Choi, G.; Prince, T.; Miao, J.; Cui, L.; Guan, W. Sample-to-Answer Palm-Sized Nucleic Acid Testing Device towards Low-Cost Malaria Mass Screening. *Biosens. Bioelectron.* **2018**, *115*, 83−90.

(39) Ma, Y.-D.; Li, K.-H.; Chen, Y.-H.; Lee, Y.-M.; Chou, S.-T.; Lai, Y.-Y.; Huang, P.-C.; Ma, H.-P.; Lee, G.-B. A Sample-to-Answer, Portable Platform for Rapid Detection of Pathogens with a Smartphone Interface. *Lab. Chip* **2019**, *19* (22), 3804−3814.

(40) Seo, J.; Sim, Y.; Kim, J.; Kim, H.; Cho, I.; Nam, H.; Yoon, Y.-G.; Chang, J.-B. PICASSO Allows Ultra-Multiplexed Fluorescence Imaging of Spatially Overlapping Proteins without Reference Spectra Measure-ments. *Nat. Commun.* **2022**, *13* (1), 2475.

(41) Huerta, J. M.; Pirbhai, M. Exploring the Potential of a Multispectral-Sensing System With Automated Machine Learning for Multiplex Detection. *IEEE Sens. J.* **2023**, *23* (19), 22600−22607.

(42) Goncharov, A.; Joung, H.-A.; Ghosh, R.; Han, G.-R.; Ballard, Z. S.; Maloney, Q.; Bell, A.; Aung, C. T. Z.; Garner, O. B.; Carlo, D. D.; Ozcan, A. Deep Learning-Enabled Multiplexed Point-of-Care Sensor Using a Paper-Based Fluorescence Vertical Flow Assay. *Small* **2023**, *19* (51), 2300617.

(43) Cortes, C.; Vapnik, V. Support-Vector Networks. *Mach. Learn.* **1995**, *20* (3), 273−297.

(44) Leal, A. L.; Silva, A. M. S.; Ribeiro, J. C.; Martins, F. G. Using Spectroscopy and Support Vector Regression to Predict Gasoline Characteristics: A Comparison of 1H NMR and NIR. *Energy Fuels* **2020**, *34* (10), 12173−12181.

(45) Murtagh, F. Multilayer Perceptrons for Classification and Regression. *Neurocomputing* **1991**, *2* (5), 183−197.

(46) Notomi, T.; Okayama, H.; Masubuchi, H.; Yonekawa, T.; Watanabe, K.; Amino, N.; Hase, T. Loop-Mediated Isothermal Amplification of DNA. *Nucleic Acids Res.* **2000**, *28* (12), No. 63e.

(47) Tanner, N. A.; Zhang, Y.; Evans, T. C. Simultaneous Multiple Target Detection in Real-Time Loop-Mediated Isothermal Amplifica-tion. *BioTechniques* **2012**, *53* (2), 81−89.

(48) Armbruster, D. A.; Pry, T. Limit of Blank, Limit of Detection and Limit of Quantitation. *Clin. Biochem. Rev.* **2008**, *29* (Suppl1), S49−S52.

(49) Broughton, J. P.; Deng, X.; Yu, G.; Fasching, C. L.; Servellita, V.; Singh, J.; Miao, X.; Streithorst, J. A.; Granados, A.; Sotomayor-Gonzalez, A.; Zorn, K.; Gopez, A.; Hsu, E.; Gu, W.; Miller, S.; Pan, C.-Y.; Guevara, H.; Wadford, D. A.; Chen, J. S.; Chiu, C. Y. CRISPR-Cas12-Based Detection of SARS-CoV-2. *Nat. Biotechnol.* **2020**, *38* (7), 870−874.

(50) Zhang, Y.; Tanner, N. A. Development of Multiplexed Reverse-Transcription Loop-Mediated Isothermal Amplification for Detection of SARS-CoV-2 and Influenza Viral RNA. *BioTechniques* **2021**, *70* (3), 167−174.

(51) Takayama, I.; Nakauchi, M.; Takahashi, H.; Oba, K.; Semba, S.; Kaida, A.; Kubo, H.; Saito, S.; Nagata, S.; Odagiri, T.; Kageyama, T. Development of Real-Time Fluorescent Reverse Transcription Loop-Mediated Isothermal Amplification Assay with Quenching Primer for Influenza Virus and Respiratory Syncytial Virus. *J. Virol. Methods* **2019**, *267*, 53−58.